Optical Gain of Lead Halide Perovskites Measured via the Variable Stripe Length Method: What We Can Learn and How to Avoid Pitfalls

Optical Gain of Lead Halide Perovskites Measured via the Variable Stripe Length Method: What We Can Learn and How to Avoid Pitfalls

*Ada Lili Alvarado-Leaños, Daniele Cortecchia, Giulia Folpini, Ajay Ram Srimath Kandada, and Annamaria Petrozza**

In the search for novel photonic materials, the recent focus on metal halide perovskites (MHPs) has revealed their promise to become groundbreaking low-threshold, tunable coherent light sources. An accurate determination of the optical gain coefficient (g) would help to screen for materials and design highly efficient perovskite lasers. Nevertheless, contradictory numbers are continuously reported, making this figure of merit unreliable. To address this issue, the present work outlines a meticulous analysis to retrieve g of $MAPbI_3$, based on the variable stripe-length (VSL) method. This method is often preferred due to its apparent simplicity; however, one can arrive at incorrect conclusions without the adequate considerations. Therefore, here the experimental implementation and numerical treatment of the data are thoroughly discussed to establish a robust VSL methodology. The obtained power dependence and spectral gain evolution point to the role of electron– hole bimolecular recombination dictating the stimulated emission properties of MAPbI3, with a behavior resembling that of bulk GaAs. Beyond providing further knowledge on the procedure to carry out pertinent VSL measurements, this work also outlines a meticulous methodology to study the underlying photophysical gain properties of MHPs and consequently, to obtain a deeper understanding of the lasing properties of these complex materials.

1. Introduction

hole bimolecular recombination dictating the stimulated emission properties of MAPbI3, with a behavior resembling that of bulk GaAs. Beyond providing further knowledge on the procedure to carry out pertinent VSL measurements, this work also outlines a meticulous methodology to study the underlying photophysical gain properties of MHPs and consequently, to obtain a deeper understanding of the lasing properties of these complex materials.Metal halide perovskites (MHPs) have recently emerged as promising light sources, due to their unique optoelectronic properties.[1–3] Ever since the first reports on room tempera- ture amplified spontaneous emission (ASE) as well as lasing in 3D perovskites, the remarkable potential of MHPs, as coherent light sources, has become increasingly evident.[4,5] Thus prompting the development of a wide variety of perovskite laser micro and nanostructures,[G–8] such as distributed feedback lasers,[9,10] vertical cavities, photonic crys- tals, among others.[11–15] These systems have made it possible to obtain ultra- low lasing pumping thresholds, down to 220 nJ cm^{-2} and quality factors above 1000 under pulsed optical excitation,[1G,17] which even challenge the performance of epitaxially grown inorganic semiconduc- tors. Among the optical and electronic characteristics that have fostered the rise of perovskite light sources are: high photo- luminescence quantum yield at high excitation density,[4] long radiative recom- bination lifetime up to hundreds of ns,[18] sharp absorption edges, high absorption coefficient and low trap densities.[19,20] Furthermore, the chemical versatility allows luminescence tuning from UV to NIR,[21,22] also covering the "green gap" where InGaN/AlGaN materials undergo efficiency roll-off.[23] MHPs, as ionic solids, can be easily processed from solution and vapor-based techniques maintaining high compatibly with traditional organic and inorganic semiconductors, thus being ideal candidates for on-chip integration including comple- mentary metal oxide semiconductor (CMOS) backplanes.[24–27] Recent reports of optically pumped lasing under CW condi- tions,[28–31] together with advances in perovskite light emitting diodes, operating in a regime of high current densities, have positioned MHPs as promising candidates for the realization of electrically pumped laser diodes.[32–35]

Despite the rapid technological advances, fundamental photo- physical processes underlying lasing in MHPs are not yet fully understood. The impact of many-body effects at high excitation densities, as well as the role of excitonic correlations and elec- tron–hole plasma recombination beyond the Mott transition, in determining the lasing thresholds are still debated.[G,3G–40] Optical gain is a key factor that determines the lasing poten- tial of a material, where a positive optical gain is required to achieve lasing. The optical gain coefficient, g, which quantifies the amount of light amplified per unit length, is an impor- tant figure of merit for the accurate design and optimization of lasers.[41,42] Precisely determining optical gain as a function of pump characteristics, excitation density, and temperature, can provide relevant insights into the mechanism of stimu- lated emission and the material factors that govern it. Thus, the

A. L. Alvarado-Leaños, Dr. D. Cortecchia, Dr. G. Folpini, Dr. A. Petrozza
Center for Nanoscience and Technology@PoliMi
Istituto Italiano di Tecnologia, via Giovanni Pascoli 70/3, Milano 20133, Italy E-mail: Annamaria.Petrozza@iit.it
Dr. A. R. Srimath Kandada
Department of Physics and Center for Functional Materials
Wake Forest University Winston-Salem, NC 27109, USA

optical gain coefficient could be a useful parameter to investigate materials, as well as for thin film processing screening.[43] However, its estimation is a complex endeavor, which could benefit from a simple and unambiguous methodology.[44]

Among the different approaches to estimate the optical gain coefficient of a material, the variable stripe-length (VSL) method is one of the most widely used techniques. In this method, a thin film semiconductor is optically pumped by a stripe-shaped beam and the amplified spontaneous emission (ASE) signal is collected from the film's edge.[45,4G] The stripe acts as an optically pumped waveguide, which amplifies the sample's luminescence. By quantitatively analyzing the change of the ASE intensity, as a function of the stripe length (z), the optical gain coefficient can be determined.

Estimations of the optical gain coefficient using the VSL method, span from 12.9 to 450 cm^{-1}, for 3D MHPs.[5,21,22,24,2G,39,47–52] In the case of $MAPbI_3$, the reported values typically fall within 70 and 370 cm^{-1},[5,24,49,51,53,54] while complementary transient absorption methods have estimated an optical gain coefficient as high as 3200 cm^{-1}.[55] Such widespread range of gain values may simply be correlated to the material quality and thickness resulting from the thin film processing, or different experimental conditions (e.g., excitation density, pump energy, repetition rate). However, additional uncertainties may also arise due to the lack of a well-founded VSL methodology.[43,45] At present, the reported VSL experimental implementation and data analysis appear to show inconsistencies, where, for example, the VSL curve is fitted at different stripe length ranges. If the VSL method is chosen to extract the optical gain coefficient, it is fundamental to consider that, both the experimental implementation and numerical retrieval of *g*, presents pitfalls that must be avoided as to obtain a reliable estimation. Indeed, a precise calculation of g is essential to identify the more promising materials and gives further insight into the performance of perovskites as lasing materials.

This work highlights the experimental requirements and analytical methods to obtain reliable optical gain coefficient values by investigating the archetypal perovskite, $MAPbI_3$. Such analysis enabled the investigation of the optical gain of $MAPbI_3$ as a function of pump power, including the optical gain spectral shape evolution at different excitation densities. The consistent determination of the optical gain coefficient allowed the identification of a behavior, which is reminiscent of bulk GaAs-like semiconductor, where light amplification is dictated by an electron–hole bimolecular recombination process. These results can shed light on fundamental $MAPbI_3$ gain properties, which are relevant in the design and development of perovskite-based lasers, while supporting a more comprehensive analysis of the mechanisms underlying lasing in MHPs.

2. Results and Discussion

The PL emission from the studied $MAPbI_3$ thin film, illuminated with a green pump (λ_{pump} = 532 nm) of variable fluence, is shown in **Figure 1**a. For low fluences, the sample luminescence has the typical PL spectrum of $MAPbI_3$, with a peak around 7G5 nm. As the pump fluence is increased, in the spectral region of higher optical gain, a narrower ASE feature emerges at 785 nm, where the intensity (Figure 1b, blue triangles, left scale) grows rapidly on the onset of ASE. Concurrently, the ASE peak narrows, as reflected by the abrupt drop of the full width half maximum (FWHM, red squares, right scale) from 75 to 8 nm. The amplification threshold is identified to be at I_{thr} = 46.21 μJ cm^{-2}, as given by the zero crossing of the fitted line of the ASE intensity as a function of pump fluence (dashed blue line). At higher pump fluences ($I_{pump} \approx$ 350 μJ cm^{-2}), the linear growth is no longer observed due to ASE saturation.

2.1. A Robust VSL Set-Up

The experimental setup, as sketched in **Figure 2**a, primarily consists of i) a coherent light source, here a picosecond pulsed laser, ii) a cylindrical lens (Cyl) to focus the Gaussian beam onto a stripe-shaped beam on the sample, iii) a movable slit, which defines the excitation stripe length and iv) a PL collection system perpendicularly aligned to the excitation plane. Even though the implementation of the experimental setup appears to be straightforward, several aspects must be taken into consideration to mitigate artefacts in the measurement, such as: i) diffraction pattern contributions arising from the interaction

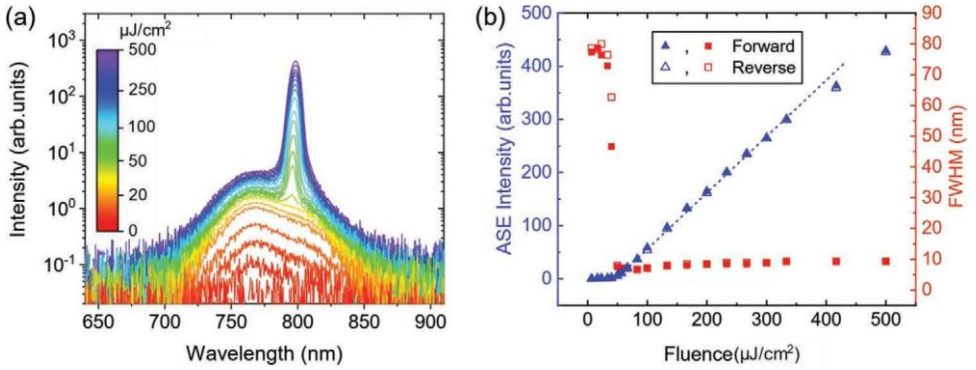

Figure 1. ASE fluence dependent behavior of a $MAPbI_3$ thin film. a) Photoluminescence spectra as a function of fluence: a narrow ASE feature appears on top of the PL emission for 50 μW cm^{-2} (light green). b) ASE intensity (blue triangles, left axis) and FWHM (red squares, right axis). To exclude photodegradation, both forward and reverse measurements were performed, which are respectively shown as closed and open symbols. The fitted ASE intensity as a function of fluence (dashed blue line) gives an ASE threshold of I_{thr} = 46.21 μJ cm^{-2}.

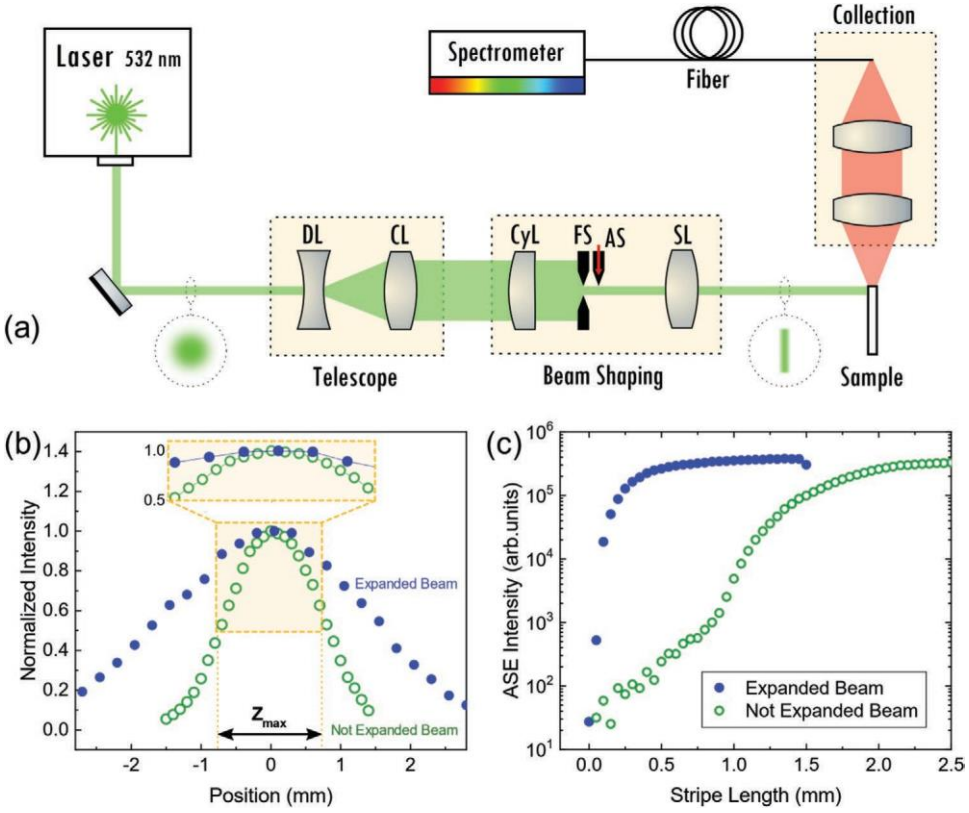

Figure 2. a) Experimental set-up for an adequate VSL measurement: a Gaussian laser beam is expanded to a diameter much larger than the desired maximum stripe length (z_{max}) by using a telescope system, consisting of a diverging lens (DL) and a converging spherical lens (CL). A cylindrical lens (Cyl) focuses the beam on an adjustable slit (AS), while a fixed slit (FS) cuts the tails of the beam. A biconvex spherical lens (SL) images the slit on the sample, positioned at normal incidence. The photoluminescence is collected from the side of the sample and sent to an optical fiber coupled to a spectrometer. b) Comparison of the beam shape on the sample obtained with (filled blue circles) or without (open green circles) the expander telescope. Within the central area of 1.5 mm (maximum stripe length) the power varies from 50% of the peak power (not expanded beam) to 10% (expanded beam). c) VSL curves obtained when using the expanded (filled blue circles) and not expanded (open green symbols) beam profiles.

of the laser beam with the edge of the slit, which must be minimized so that tail diffraction patterns in the beam profile become negligible, ii) the need for a uniform pump intensity along the entire illuminating stripe, in which a good approximation to a top-hat excitation profile is required, iii) optimal outcoupling of the ASE signal.

Firstly, in the VSL method, diffraction effects are problematic as they can give rise to artificial positive optical gain coefficient values.[5G] The presence of the slit makes the existence of diffraction patterns unavoidable. Nevertheless, by placing the slit and the sample very close to each other, diffraction can be minimized. However, since this configuration is often not possible to implement, an alternative approach is to project, the light passing through the slit, onto the sample using a spherical lens (SL in Figure 2a). Changing the magnification of the imaging system, by adjusting the position of the SL, provides a way to fine tune the stripe size on the sample.[57]

Secondly, the uniformity of the pump intensity must be optimized given that the VSL technique is designed for an excitation source with a uniform intensity profile. The lasers that are frequently employed in VSL setups, possess a Gaussian spatial profile that is preserved on the horizontal intensity profile of the stripe that illuminates the sample. The beam profile in the focal plane is Gaussian along each direction, where the vertical width is determined by the magnification of the optical system and the horizontal width is the same as the one from the incoming beam (Figures S2 and S3, Supporting Information). Typically, to perform a VSL measurement, stripe lengths of several hundreds of microns to a couple of millimeters are used. A standard laser output (Figure 2b, open green circles) has a radius of around $r_{(1/e)} \approx 1$ mm. Assuming a maximum stripe length of $z_{max} = 1.5$ mm, the pump power at the edges of the stripe decreases by 50% of the maximum power in the center (see inset). This inevitably affects the shape of the VSL curve (Figure 2c, open green circles), resulting in a slower intensity growth that is essentially a consequence of the lower effective fluence. This shows how an analysis that relies on a non-uniform profile will lead to an incorrect estimation of the optical gain coefficient. Furthermore, the initial sub-exponential growth (Figure 2c) can be incorrectly interpreted as a consequence of the material's response, for instance due to biexcitonic effects, while in reality this could be simply due to the incorrect beam profile – a geometrical artefact. Therefore, it is essential to adjust the optical setup to achieve a uniform beam shape within the pertinent stripe length range. In this regard, the initial laser beam is expanded such that the desired maximum stripe length, z_{max}, falls within a central part of the Gaussian beam where the intensity profile is relatively flat. Beam expansion is achieved by adding a telescope section (DL

and CL in Figure 2a), where the output beam would have $r_{(1/e)} \approx$ 2 mm on the cylindrical lens. The result is that the horizontal beam profile on the sample (Figure 2b, closed blue circles) drops by about 10% of the central intensity, at the edges of a 1.5 mm stripe. To ensure that only the central part of the beam is used, a fixed slit is positioned (FS) at the center of the Gaussian profile with the desired z_{max} aperture at the focus of Cyl. An adjustable slit (AS) mounted on a motorized precision stage is then used to vary the stripe length. The position of the sample is manually adjusted so that the illuminating stripe falls on the sample's edge. Figure 2c compares the VSL curves of the expanded and not expanded Gaussian beams, where the expanded beam shows, for small stripe lengths, a steeper exponentially growth. Furthermore, for the expanded beam configuration, the onset of gain saturation, at $z \approx 300$ μm, is reached sooner than for the not expanded case. While in-depth discussion of the modeling will be presented in the next section, for the moment it is worth mentioning that from the linear amplifier model an optical gain coefficient of $g = 700$ cm^{-1} can be extracted. Meanwhile, attempting to apply the same analysis to the not expanded Gaussian beam results in a value of $g = 120$ cm^{-1}. This clearly illustrates that a fundamental condition of the VSL method is to illuminate the sample with a homogenous stripe. Therefore, the initial slow rise and less steep exponential growth of the VSL curve (Figure 2c, green open circles) represent artefacts, given that they stem from a non-uniform beam, which does not conform to the requirements to the VSL measurement. Consequently, the apparent slower increase of the ASE intensity results in a significant underestimation of the optical gain coefficient. Overall, this shows that a uniform pump intensity over the entire stripe length is essential to avoid an artificial spatial dependence of the optical gain coefficient, which can lead to incorrect conclusions.[5G]

Thirdly, the remaining aspect to consider here is the PL collection geometry. To collect preferentially radiation amplified in the 1D waveguide created by the stripe, PL is collected not from the front of the sample but from the side. Thus, the sample is positioned perpendicularly to the pump beam, with the collection line located at a right angle and in the focal plane of the imaging system. The output ASE radiation coming from the side of the sample must be adequately coupled to the collection line to obtain a constant coupling while varying the size of the stripe.[5G] The collection line needs to be aligned so that its source is positioned at the very edge, and not further inside the thin film. To ensure that no artefacts are present, a shifting excitation spot (SES) measurement is performed, before continuing with the VSL measurement (Figure S4, Supporting Information). In this technique, a small slit aperture that creates the excitation spot, is moved from the edge of the sample toward the center. In the absence of artefacts, the collected PL decreases further from the sample's edge due to reabsorption losses, which can be estimated from the Beer-Lambert law $I_{SES}(z) \approx e^{-\alpha z}$, where α is the optical absorption coefficient. From the SES measurement, using a slit size of 0.15 mm, the fitting of the curve in Figure S4 (Supporting Information) resulted in $\alpha = 9.$ cm^{-1}.

Once the optical VSL setup was optimized, VSL measurements were performed for a variety of excitation densities. The following section presents the quantitative methodology used to extract the optical gain coefficient.

2.2. Extracting the Optical Gain Coefficient

In this section, the methodology for extracting the optical gain coefficient is outlined in terms of a VSL measurement at an input fluence of ≈70 μJ cm^{-2}, which is above the ASE threshold (see Figure 1). The ASE peak intensity and its corresponding FWHM as a function of the stripe length are shown in **Figure 3**a. An increase of the stripe length results in a clear exponential growth of the ASE intensity along with a substantial spectral narrowing. This trend stops as the stripe length is increased and saturation is reached, where the FWHM stabilizes and the ASE growth becomes subexponential. From the VSL curve (Figure 3a, red curve), the optical gain coefficient can be retrieved, nevertheless a careful analysis of the VSL data is required to obtain robust theoretical results. For example, saturation needs to be accounted for, by identifying the stripe length and pump intensity regimes associated with the saturation onset. In this regard, the VSL data is fitted and analyzed using two models: 1) the small-signal gain (SSG) model, where gain saturation is neglected, and 2) the gain saturation (Gsat)

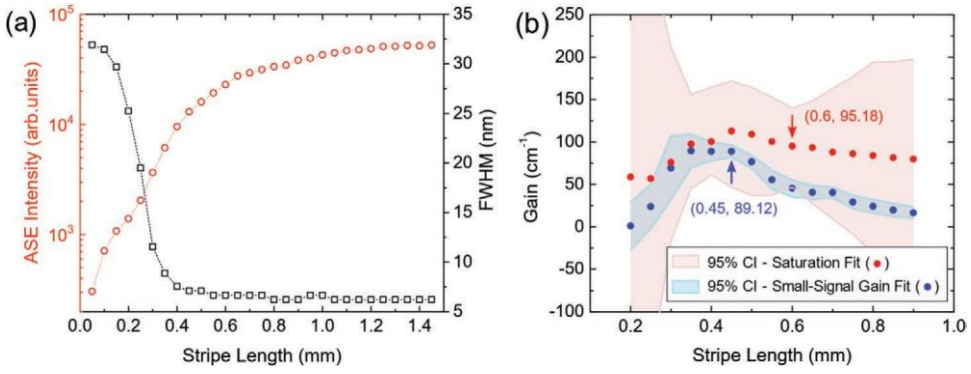

Figure 3. a) VSL curve (red open circles, left axis) for an input fluence of $I_{pump} = 67$ μJ cm^{-2} and the corresponding FWHM (open black rectangles, right arrow). b) Optical gain coefficient as a function of the fitted stripe length range, calculated using the small-signal gain model (blue circles) and the saturation model (red circles), with its corresponding 95% confidence interval (95% CI). The arrows indicate the best fits of $g = 89.12$ cm^{-1} for $z_{lim} = 0.45$ mm, and $g = 95.18$ cm^{-1} for $z_{lim} = 0.6$ mm, for the SSG and the Gsat models, respectively.

model. The advantages and disadvantages of each model are discussed and, it is shown that, after a detailed analysis, both models can give reliable fitting results, albeit each one within its own respective stripe length ranges.

As a first approximation, the excited region is considered a single pass 1D amplifier for the photons propagating within the stripe. The resulting light amplification leads to an exponential growth of the ASE intensity as a function of the stripe length, z, as given by the small-signal gain model[58]

$$I_{\mathrm{ASE}}(z) = \frac{A_{\mathrm{sp}}(\Omega)}{g}\left(e^{gz} - 1\right) \quad (1)$$

where g is the optical gain coefficient, $A_{\mathrm{sp}}(\Omega)$ accounts for the spontaneous emission intensity and the collection solid angle Ω. The SSG model assumes that the optical gain coefficient is constant along the entire excitation region, and thus independent of the stripe length. At higher excitation intensities, however, saturation sets in, resulting in a subexponential ASE growth and in an effective gain that depends on the stripe length, z. To account for saturation, Equation (1) can be modified to consider the dependence of gain on the excitation intensity, as described by the gain saturation model[56]

$$\frac{dI_{ASE}}{dz} = \frac{gI_{ASE}}{1 + \frac{I_{ASE}(z)}{I_{sat}}} + A_{sp}(\Omega)\frac{1}{1 + \frac{I_{ASE}(z)}{I_{sat}}} \quad (2)$$

where I_{sat} is the saturation intensity, corresponding to the ASE intensity at which saturation is reached.

To determine the optical gain coefficient more accurately, it is necessary to study how the size of the stripe length affects the calculated gain.[43] By analyzing the dependence of the optical gain coefficient on the stripe length, it becomes possible to identify the stripe length at which saturation is reached, known as the saturation length z_{sat}. With this information, one can establish the region where the SSG model is valid and where it becomes unavoidable to use the Gsat model.

Figure 3b shows how the estimated optical gain coefficient changes as a function of the stripe length, when fitting the VSL experimental data from Figure 3a, at a pump fluence of I_{pump} = 67 μJ cm^{-2}. The fits, using both the SSG model and the Gsat model, were performed with progressively increasing stripe lengths, all starting from z_0 = 0.02 cm and ending at a variable stripe length z_{fit}. The closed circles represent the value of the calculated g from a fit up to z_{fit}, while the shaded area indicates the 95% confidence interval (CI) of the fit of g. For the SSG model a clear pattern is observed, where for the smallest stripe lengths, the gain value increases, and the CI is large. At the central region (350 μm < z < 450 μm) the calculated gain remains relatively constant, while the CI progressively decreases to a minimum. For larger stripe lengths, the decrease of the calculated g and the increase of the CI as well as the FWHM (Figure 3a) saturation, indicate that gain saturation has been reached at $z_{\mathrm{sat}} \approx 0.045$ cm. After this stripe length (when $z > 0.045$ cm), the SSG model is no longer valid, and the Gsat model must be used.[5G] Beyond the saturation length, the fit of the Gsat model gives a minimum CI at $z = 0.06$ cm, with a corresponding $g = 95.18$ cm^{-1} (red arrow). Meanwhile, for the SSG model, at z = 0.045 cm, where the smallest CI is obtained before reaching the region where the optical gain coefficient starts to decrease, the fit gives $g = 89.12$ cm^{-1} (blue arrow). Therefore, both models are complementary, when used within the adequate stripe length range. Nevertheless, the large CI obtained with the Gsat model makes it clear that the additional parameters of the Gsat model add complexity, thus giving rise to a less stable fit.

The VSL curves corresponding to different pump fluences are presented in Figure 4a, showing the expected exponen- tial growth before the saturation onset. The curves become steeper as the pump fluence is increased, illustrating how the optical gain coefficient varies with pump fluence. Using the VSL curves from Figure 4a, the fluence-dependent gain is determined by fitting both the SSG model (black rectangles) and the Gsat model (red circles), as shown in Figure 4b. For lower fluences, the calculated optical gain coefficient values are consistent. In contrast, for higher pump fluences, the increase of the ASE intensity before z_{sat} is too steep to reliably calculate the optical gain coefficient with the SSG model. However, the gain value can still be determined using the Gsat model, given that this approach considers a wider stripe length range. From this point of view, the error analysis presented here is essential to identify the fluence regime where the exponential SSG model is applicable, and at which fluence

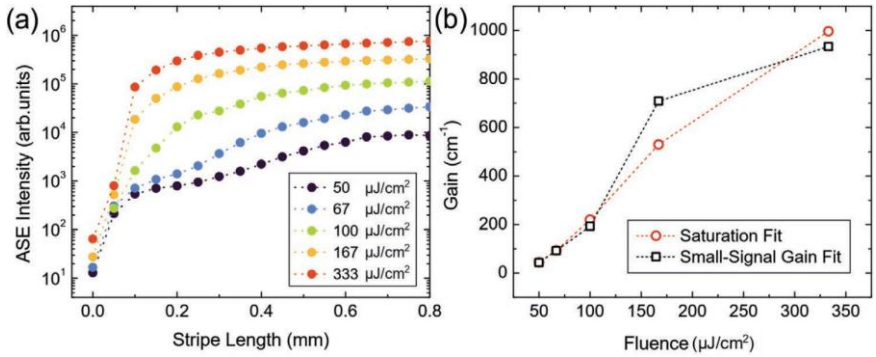

Figure 4. a) Fluence dependence of the VSL curve from 50 to 333 μJ cm^{-2}. b) Fluence dependent gain calculated using the SSG model (open black rectangles) and the Gsat model (open red circles).

values it becomes necessary to use the approach in which saturation is explicitly considered. This analysis would provide a more robust determination of the stopping fit stripe length, z_{fit}, which gives a more reliable estimation of the optical gain coefficient.

2.3. Discussion: ASE and the Optical Gain Coefficient of a $MAPbI_3$ Thin Film

Up to this point, a robust procedure to retrieve the optical gain coefficient has been outlined. A further consideration is that the ASE spectrum varies with both stripe length and pump fluence. At low fluences, below the ASE threshold, a double-peak feature, at 765 and 795 nm, is observed in the spontaneous emission collected from the edge of the studied sample (Figure S5, Supporting Information). The existence of a double peak PL spectrum in lead halide perovskite thin films has been previously reported and analyzed.[59] The power dependence of the peak at 765 nm and the ASE peak at 795 nm follow different trends. This discrepancy could be attributed to a variety of contributions, such as the presence of two different emissive species, reabsorption or other optical effects due to the VSL configuration.[G0] Given that the spectral evolution around 7G5 nm does not follow a characteristic ASE behavior it is not further discussed here, as it is not the focus of this work (Figure SG, Supporting Information). As a result, the spectral gain is analyzed within the window of 785–807 nm, where ASE is present (**Figure 5**). Figure 5a–c shows the ASE spectra as a function of z for three different pump fluences (100, 67, and 50 μJ cm^{-2} respectively). The wavelength dependence of the optical gain coefficient is characterized by a distinct spectral gain g_λ, which is estimated by fitting the SSG model to the VSL curvesrom a series of spectral positions between 78G and 807 nm. The resulting gain spectra for the three powers are presented in Figure 5d. The gain spectrum of the lowest fluence has a maximum around 795 nm, while for higher pump fluences, a blue shift of the gain spectrum maximum of up to 2 nm is observed. The behavior is consistent with the free carrier gain model for a 3D semiconductor (e.g., bulk GaAs), where the excited species responsible for optical gain consist primarily of free carriers with minimal excitonic contribution.[44] As the pump intensity is increased, resulting in a higher carrier density, the spectral gain is expected to extend further to the blue, with a corresponding blue shift of the stimulated emission spectrum, which is indeed observed in the calculated spectral gain (Figure 5d).

By comparing the spectral gain (Figure 5d) to the individual PL spectra (Figure 5a–c), it can be seen that the maximum gain corresponds to the region where the largest increase in intensity between consecutive PL spectra is observed. Meanwhile, after the onset of saturation, the spectra of Figure 5a show a clear red shift. The spectra of Figure 5a indicate that saturation is reached faster for shorter wavelengths. Thus, after saturation takes place for the shorter wavelengths, increasing the stripe length still results in an increase of the emitted light, however the emission dominates on the red side of the spectrum, where higher input fluences are required to reach saturation.

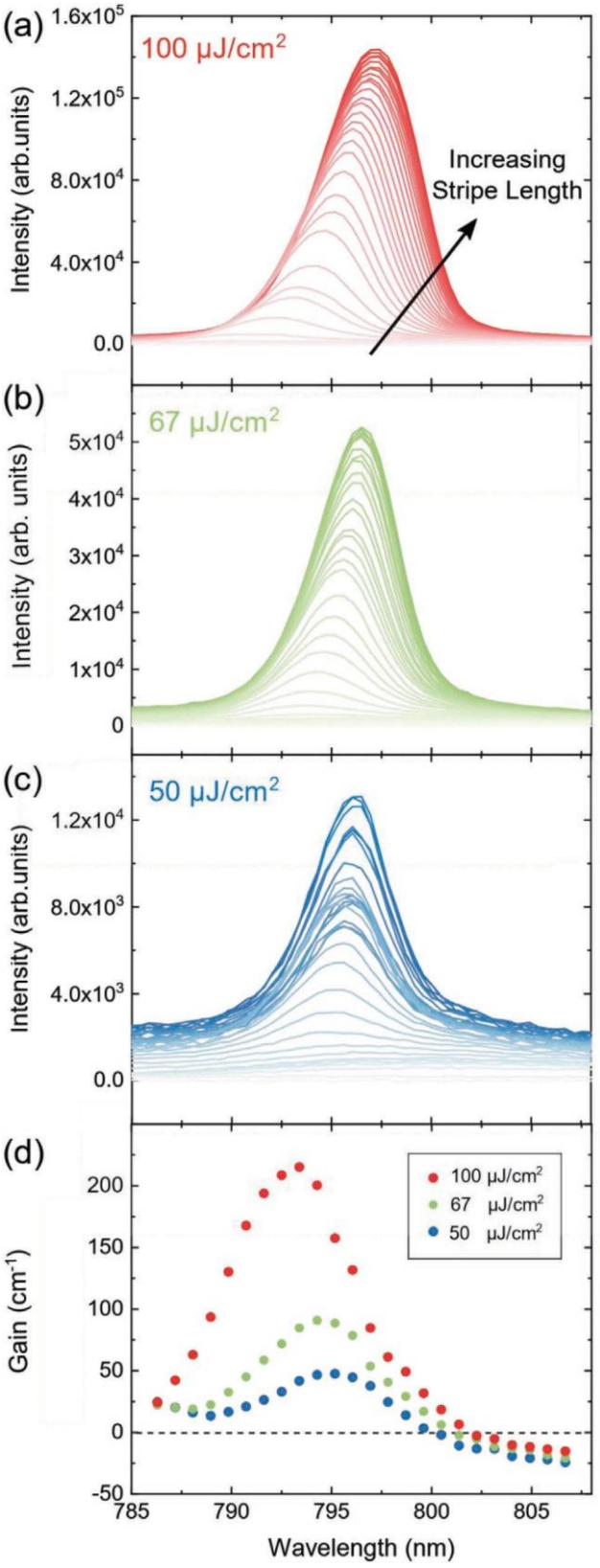

Figure 5. a-c) Spectra for different stripe lengths with $I_{pump} = 100$, 67, and 50 μJ cm^{-2} respectively. d) Gain spectra for $I_{pump} = 50$, 67, and 100 μJ cm^{-2}.

3. Conclusion

This work provided a judicious analysis of the gain properties of $MAPbI_3$ by means of the VSL method. It has been shown that a robust VSL set-up with a uniform intensity profile excitation impinging on the sample and optimized collection coupling is required to obtain adequate VSL curves, which would otherwise compromise the accuracy of the results. Equally important, to retrieve a reliable optical gain coefficient, a careful analysis of the VSL data must be performed, while considering the onset of gain saturation. In this regard, supported by a detailed error analysis, the SSG model and the Gsat model were compared. Furthermore, the appropriate intensity regimes and optimal stripe length used for fitting the VSL data (z_{lim}), in which each model can give a reliable gain value, were analyzed. Having established a rigorous methodology, the gain properties of $MAPbI_3$ were investigated as function of the excitation density. The observed characteristic gain power dependence and gain spectral evolution can be interpreted in the framework of electron–hole bimolecular recombination in 3D semiconductors, which resembles the behavior of GaAs. Our study would help to establish a basis for the analysis of the photophysics underlying the gain properties of MHPs. This could enable a more detailed and systematic analysis to understand how the gain properties of perovskites are influenced by temperature, excitation pulse-width repetition rate, as well as the material processing. Furthermore, the methodology described here is not limited to MHPs, but can be rather applicable to the analysis of the gain properties of a wide range of emerging semiconductor materials.

4. Experimental Section

Synthesis: Methylammonium lead iodide ($MAPbI_3$) thin films with thickness 141 ± 4 nm and roughness (R_a) of 4 ± 1 nm were fabricated with the spin-coating technique. Lead iodide (PbI_2, 99.999%) and methylammonium iodide (MAI > 98%) were purchased from TCI and Dyesol, respectively. Anhydrous dimethyl sulfoxide (DMSO, 99.9%) and Dimethylformamide (DMF, 99.8%) were purchased from Sigma-Aldrich. In a typical process PbI_2, MAI, and DMSO (1:1:1 molar ratio) were mixed in DMF to obtain a precursor solution at a concentration of 0.7 M. Glass substrates were cleaned by sonication in acetone, deionized water and isopropanol and then treated with oxygen plasma. The perovskite precursor solution was spin-coated on a glass substrate at 6000 rpm for 30 s. After 6 s from the beginning of the process, 200 μL of chlorobenzene (Sigma Aldrich, anhydrous, 99.8%) were dropped on the sample. The film was annealed on a hotplate at 100 °C for 15 min. The fabrication process was performed in a glovebox under N_2 atmosphere. The films were characterized with a surface profiler Dektak 150 (Veeco), while X-ray diffraction (XRD) was performed with a BRUKER D8 ADVANCE with Bragg-Brentano geometry, using Cu Kα radiation (λ = 1.54056 Å), step increment of 0.02° and 1 s of acquisition time (Figure S1a, Supporting Information). Steady state absorption was acquired (Figure S1b, Supporting Information) on a UV/VIS/NIR spectrophotometer Lambda 1050, Perkin Elmer equipped with an integrating sphere (module 150 mm InGaAs Int. Sphere).

Static PL and Threshold Measurement: Photoluminescence spectra were acquired using as excitation source a pulsed 532 nm green laser (Innolas Picolo 2nd harmonic), with a pulse duration of 800 ps and a repetition rate of 1 kHz. The laser fluence on the sample was varied using a filter wheel. A cylindrical lens (f = 100 mm) was used to focus the beam on a 1.5 mm slit to create a stripe that was imaged on the sample by a biconvex lens (f = 50 mm). The beam-expander telescope was comprised of a diverging (f = −100 mm) and a converging lens (f = +200 mm) set at a distance d = 80 mm, to achieve a magnification M = 2. The result was a collimated beam at the output, which compensated the divergence of the incoming laser. The adjustable slit (AS) was placed on the side of the sample edge to account for the horizontal plane reflection caused by the imaging system.

The sample was kept in a controlled nitrogen atmosphere to avoid degradation due to contact with oxygen or water vapor in air. Photoluminescence was collected with a fiber coupled Maya 1000 spectrometer (1 nm resolution) after filtering the pump radiation using a 650 nm long-pass filter. The ASE threshold was measured by varying the input fluence and measuring the output spectrum.

Variable Stripe Length Method: The set-up previously described for the threshold measurements was also used to obtain the VSL data, with the addition of a razor blade on a motorized stage to vary the size of the illumination stripe arriving on the sample. A fixed slit blocked the tails of the expanded laser beam, thus ensuring that only the central beam was used to excite the sample. The collection line was optimized for collecting PL from the edge of the sample, while using a sample that was cleaved at the center to ensure a uniform surface and minimum scattering. The beam profiles were measured at the slit and sample position through the knife edge technique.

Supporting Information

Supporting Information is available from the Wiley Online Library or from the author.

Acknowledgements

A.P. and G.F. acknowledge funding from ERC project SOPHY under grant agreement N 771528, D.C. acknowledges funding from MSCA grant agreement No 839480 (PERICLeS).

Conflict of Interest

The authors declare no conflict of interest.

Keywords

metal halide perovskites, lasing, optical gain, variable stripe-length (VSL) method

[1] B. R. Sutherland, E. H. Sargent, *Nat. Photonics* **2016**, *10*, 295.

[2] S. A. Veldhuis, P. P. Boix, N. Yantara, M. Li, T. C. Sum, N. Mathews, S. G. Mhaisalkar, *Adv. Mater.* **2016**, *28*, 6804.

[3] D. Cortecchia, J. Yin, A. Petrozza, C. Soci, *J. Mater. Chem. C* **2019**, *7*, 4956.

[4] F. Deschler, M. Price, S. Pathak, L. E. Klintberg, D. D. Jarausch, R. Higler, S. Hüttner, T. Leijtens, S. D. Stranks, H. J. Snaith, M. Atatüre, R. T. Phillips, R. H. Friend, *J. Phys. Chem. Lett.* **2014**, *5*, 1421.

[5] G. Xing, N. Mathews, S. S. Lim, N. Yantara, X. Liu, D. Sabba, M. Grätzel, S. Mhaisalkar, T. C. Sum, *Nat. Mater.* **2014**, *13*, 476.

[6] H. Dong, C. Zhang, X. Liu, J. Yao, Y. S. Zhao, *Chem. Soc. Rev.* **2020**, *42*, 951.

[7] Z. Liu, J. Yang, J. Du, Z. Hu, T. Shi, Z. Zhang, Y. Liu, X. Tang, Y. Leng, R. Li, *ACS Nano* **2018**, *12*, 5923.

[8] N. Zhang, Y. Fan, K. Wang, Z. Gu, Y. Wang, L. Ge, S. Xiao, Q. Song, *Nat. Commun.* **2019**, *10*, 1.

[9] P. Brenner, M. Stulz, D. Kapp, T. Abzieher, U. W. Paetzold, A. Quintilla, I. A. Howard, H. Kalt, U. Lemmer, *Appl. Phys. Lett.* **2016**, *102*, 141106.

[10] M. Saliba, S. M. Wood, J. B. Patel, P. K. Nayak, J. Huang, J. A. Alexander-Webber, B. Wenger, S. D. Stranks, M. T. Hörantner, J. T. W. Wang, R. J. Nicholas, L. M. Herz, M. B. Johnston, S. M. Morris, H. J. Snaith, M. K. Riede, *Adv. Mater.* **2016**, *28*, 923.

[11] N. Pourdavoud, S. Wang, A. Mayer, T. Hu, Y. Chen, A. Marianovich, W. Kowalsky, R. Heiderhoff, H. C. Scheer, T. Riedl, *Adv. Mater.* **2017**, *22*, 1605003.

[12] S. Schünemann, S. Brittman, K. Chen, E. C. Garnett, H. Tüysüz, *ACS Photonics* **2017**, *4*, 2522.

[13] S. Chen, A. Nurmikko, *Optica* **2018**, *5*, 1141.

[14] N. Pourdavoud, T. Haeger, A. Mayer, P. J. Cegielski, A. L. Giesecke, R. Heiderhoff, S. Olthof, S. Zaefferer, I. Shutsko, A. Henkel, D. Becker-Koch, M. Stein, M. Cehovski, O. Charfi, H. H. Johannes, D. Rogalla, M. C. Lemme, M. Koch, Y. Vaynzof, K. Meerholz, W. Kowalsky, H. C. Scheer, P. Görrn, T. Riedl, *Adv. Mater.* **2019**, *31*, 1903717.

[15] J. Wang, P. Da, Z. Zhang, S. Luo, L. Liao, Z. Sun, X. Shen, S. Wu, G. Zheng, Z. Chen, *Nanoscale* **2018**, *10*, 10371.

[16] S. W. Eaton, M. Lai, N. A. Gibson, A. B. Wong, L. Dou, J. Ma, L. W. Wang, S. R. Leone, P. Yang, *Proc. Natl. Acad. Sci. USA* **2016**, *113*, 1993.

[17] H. Zhu, Y. Fu, F. Meng, X. Wu, Z. Gong, Q. Ding, M. V. Gustafsson, M. T. Trinh, S. Jin, X. Y. Zhu, *Nat. Mater.* **2015**, *14*, 636.

[18] V. D'Innocenzo, G. Grancini, M. J. P. Alcocer, A. R. S. Kandada, S. D. Stranks, M. M. Lee, G. Lanzani, H. J. Snaith, A. Petrozza, *Nat. Commun.* **2014**, *5*, 3586.

[19] S. De Wolf, J. Holovsky, S. J. Moon, P. Löper, B. Niesen, M. Ledinsky, F. J. Haug, J. H. Yum, C. Ballif, *J. Phys. Chem. Lett.* **2014**, *5*, 1035.

[20] L. N. Quan, B. P. Rand, R. H. Friend, S. G. Mhaisalkar, T. W. Lee, E. H. Sargent, *Chem. Rev.* **2019**, *112*, 7444.

[21] K. Roh, L. Zhao, W. B. Gunnarsson, Z. Xiao, Y. Jia, N. C. Giebink, B. P. Rand, *ACS Photonics* **2019**, *6*, 3331.

[22] S. Yakunin, L. Protesescu, F. Krieg, M. I. Bodnarchuk, G. Nedelcu, M. Humer, G. De Luca, M. Fiebig, W. Heiss, M. V. Kovalenko, *Nat. Commun.* **2015**, *6*, 9515.

[23] J. R. Harwell, G. L. Whitworth, G. A. Turnbull, I. D. W. Samuel, *Sci. Rep.* **2017**, *7*, 11727.

[24] P. J. Cegielski, S. Neutzner, C. Porschatis, H. Lerch, J. Bolten, S. Suckow, A. R. S. Kandada, B. Chmielak, A. Petrozza, T. Wahlbrink, A. L. Giesecke, *Opt. Express* **2017**, *25*, 13199.

[25] P. J. Cegielski, A. L. Giesecke, S. Neutzner, C. Porschatis, M. Gandini, D. Schall, C. A. R. Perini, J. Bolten, S. Suckow, S. Kataria, B. Chmielak, T. Wahlbrink, A. Petrozza, M. C. Lemme, *Nano Lett.* **2018**, *18*, 6915.

[26] C. H. Lin, Q. Zeng, E. Lafalce, S. Yu, M. J. Smith, Y. J. Yoon, Y. Chang, Y. Jiang, Z. Lin, Z. V. Vardeny, V. V. Tsukruk, *Adv. Opt. Mater.* **2018**, *6*, 1800474.

[27] D. Lyashenko, A. Perez, A. Zakhidov, *Phys. Status Solidi A* **2017**, *214*, 1600302.

[28] M. Cadelano, V. Sarritzu, N. Sestu, D. Marongiu, F. Chen, R. Piras, R. Corpino, C. M. Carbonaro, F. Quochi, M. Saba, A. Mura, G. Bongiovanni, *Adv. Opt. Mater.* **2015**, *3*, 1557.

[29] Y. Jia, R. A. Kerner, A. J. Grede, B. P. Rand, N. C. Giebink, *Nat. Photonics* **2017**, *11*, 784.

[30] Y. Jia, R. A. Kerner, A. J. Grede, B. P. Rand, N. C. Giebink, *Adv. Opt. Mater.* **2020**, *8*, 1901514.

[31] C. Qin, A. S. D. Sandanayaka, C. Zhao, T. Matsushima, D. Zhang, T. Fujihara, C. Adachi, *Nature* **2020**, *585*, 53.

[32] W. B. Gunnarsson, B. P. Rand, *APL Mater.* **2020**, *8*, 030902.

[33] H. Kim, K. Roh, J. P. Murphy, L. Zhao, W. B. Gunnarsson, E. Longhi, S. Barlow, S. R. Marder, B. P. Rand, N. C. Giebink, *Adv. Opt. Mater.* **2020**, *8*, 3.

[34] H. Kim, L. Zhao, J. S. Price, A. J. Grede, K. Roh, A. N. Brigeman, M. Lopez, B. P. Rand, N. C. Giebink, *Nat. Commun.* **2018**, *2*, 4893.

[35] M. Xu, Q. Peng, W. Zou, L. Gu, L. Xu, L. Cheng, Y. He, M. Yang, N. Wang, W. Huang, J. Wang, *Appl. Phys. Lett.* **2019**, *115*, 041102.

[36] T. J. S. Evans, A. Schlaus, Y. Fu, X. Zhong, T. L. Atallah, M. S. Spencer, L. E. Brus, S. Jin, X. Y. Zhu, *Adv. Opt. Mater.* **2018**, *6*, 1700982.

[37] M. Saba, M. Cadelano, D. Marongiu, F. Chen, V. Sarritzu, N. Sestu, C. Figus, M. Aresti, R. Piras, A. Geddo Lehmann, C. Cannas, A. Musinu, F. Quochi, A. Mura, G. Bongiovanni, *Nat. Commun.* **2014**, *5*, 5049.

[38] A. P. Schlaus, M. S. Spencer, K. Miyata, F. Liu, X. Wang, I. Datta, M. Lipson, A. Pan, X. Y. Zhu, *Nat. Commun.* **2019**, *10*, 265.

[39] Y. Wang, X. Li, J. Song, L. Xiao, H. Zeng, H. Sun, *Adv. Mater.* **2015**, *27*, 7101.

[40] V. D'Innocenzo, A. R. Srimath Kandada, M. De Bastiani, M. Gandini, A. Petrozza, *J. Am. Chem. Soc.* **2014**, *136*, 17730.

[41] B. Guzelturk, M. Pelton, M. Olutas, H. V. Demir, *Nano Lett.* **2019**, *12*, 277.

[42] E. Gaufrès, N. Izard, A. Noury, X. L. Roux, L. Vivien, *Carbon Nanotubes and Graphene for Photonic Applications*, Woodhead Publishing, Cambridge **2013**.

[43] L. Cerdán, *Opt. Lett.* **2017**, *42*, 5258.

[44] W. W. Chow, S. W. Koch, *Semiconductor-Laser Fundamentals: Physics of the Gain Materials*, Springer-Verlag, Berlin Heidelberg **1999**.

[45] J. Valenta, I. Pelant, J. Linnros, *Appl. Phys. Lett.* **2002**, *81*, 1396.

[46] K. L. Shaklee, R. F. Leheny, *Appl. Phys. Lett.* **1971**, *18*, 475.

[47] G. Xing, M. H. Kumar, W. K. Chong, X. Liu, Y. Cai, H. Ding, M. Asta, M. Grätzel, S. Mhaisalkar, N. Mathews, T. C. Sum, *Adv. Mater.* **2016**, *28*, 8191.

[48] H. Zhang, Q. Liao, Y. Wu, Z. Zhang, Q. Gao, P. Liu, M. Li, J. Yao, H. Fu, *Adv. Mater.* **2018**, *30*, 1706186.

[49] A. Zhizhchenko, S. Syubaev, A. Berestennikov, A. V. Yulin, A. Porfirev, A. Pushkarev, I. Shishkin, K. Golokhvast, A. A. Bogdanov, A. A. Zakhidov, A. A. Kuchmizhak, Y. S. Kivshar, S. V. Makarov, *ACS Nano* **2019**, *13*, 4140.

[50] A. Balena, A. Perulli, M. Fernandez, M. L. De Giorgi, G. Nedelcu, V. M. Kovalenko, M. Anni, *J. Phys. Chem. C* **2018**, *122*, 5813.

[51] S. Chen, C. Zhang, J. Lee, J. Han, A. Nurmikko, *Adv. Mater.* **2017**, *22*, 1604781.

[52] A. Safdar, Y. Wang, T. F. Krauss, in *European Conf. on Lasers and Electro-Optics and European Quantum Electronics Conf.*, Optical Society of America, Washington, DC **2017**, paper JSV_3_4.

[53] A. Safdar, Y. Wang, T. F. Krauss, *Opt. Express* **2018**, *26*, A75.

[54] B. R. Sutherland, S. Hoogland, M. M. Adachi, C. T. O. Wong, E. H. Sargent, *ACS Nano* **2014**, *8*, 10947.

[55] B. R. Sutherland, S. Hoogland, M. M. Adachi, P. Kanjanaboos, C. T. O. Wong, J. J. McDowell, J. Xu, O. Voznyy, Z. Ning, A. J. Houtepen, E. H. Sargent, *Adv. Mater.* **2015**, *27*, 53.

[56] L. Dal Negro, P. Bettotti, M. Cazzanelli, D. Pacifici, L. Pavesi, *Opt. Commun.* **2004**, *222*, 337.

[57] J. Valenta, K. Luterová, R. Tomasiunas, K. Dohnalová, B. Hönerlage, I. Pelant, in *Towards the First Silicon Laser*, Springer, Dordrecht **2003**, pp. 223–242.

[58] P. W. Milonni, J. H. Eberly, *Lasers*, John Wiley & Sons, Rochester, **1988**.

[59] K. Schötz, A. M. Askar, W. Peng, D. Seeberger, T. P. Gujar, M. Thelakkat, A. Köhler, S. Huettner, O. M. Bakr, K. Shankar, F. Panzer, *J. Mater. Chem. C* **2020**, *8*, 2289.

[60] K. P. Goetz, A. D. Taylor, F. Paulus, Y. Vaynzof, *Adv. Funct. Mater.* **2020**, *30*, 1910004.